

# Operando Scanning SAXS/WAXS Cell Design for Multiscale Analysis of All-Solid-State Battery Systems

Jean-Marc von Mentlen, Magdalena Fiedler, Klara Neumayr, Pronoy Dutta, Ayça Senol Gungor, Susanne Dörfler, Heinz Amenitsch, Christian Zaubitzer, Holger Althues, Vanessa Wood,\* and Christian Prehal\*

Operando X-ray scattering techniques, particularly small- and wide-angle X-ray scattering (SAXS/WAXS), have been key for elucidating the physicochemical processes governing liquid-electrolyte batteries by providing real-time insights into phase transformations and nanoscale structural evolution. However, extending these methods to all-solid-state batteries has been experimentally challenging due to high X-ray absorption and nonideal operating pressures in transmission mode. Here a novel operando electrochemical cell design is presented that enables cross-sectional scanning SAXS/WAXS measurements, while maintaining the pressure necessary for solid-state operation. Applying this scanning SAXS/WAXS technique to all-solid-state lithium-sulfur batteries, it enables simultaneous mapping of the crystalline phase evolution and

the nanoscale structural changes across distinct cell components during cycling. Spatially resolved WAXS revealed significant heterogeneity in the formation and distribution of Li<sub>2</sub>S within the composite cathode. Simultaneously, WAXS captured an anisotropic lithiation mechanism in the Li-In anode, evidenced by the preferential disruption of In(110) planes and suggesting amorphous LiIn formation. Combined analysis of stable SAXS profiles and WAXS-derived Li<sub>2</sub>S nanocrystallite sizes suggest that the sulfur conversion occurs within the nanopores of the templated carbon host. Control experiments using a liquid-electrolyte Li-S system validated the technique's sensitivity to detect expected nanoscale changes, confirming the genuineness of the solid-state observations.

J.-M. von Mentlen, A. Senol Gungor, V. Wood  
Department of Information Technology and Electrical Engineering  
ETH Zürich  
Gloriastrasse 35, 8092 Zürich, Switzerland  
E-mail: vwood@ethz.ch

M. Fiedler  
Chair of Inorganic Chemistry I  
TUD Dresden University of Technology  
Bergstraße 66, 01062 Dresden, Germany

K. Neumayr, P. Dutta, C. Prehal  
Department of Chemistry and Physics of Materials  
University of Salzburg  
Jakob-Haringer-Straße 2a, 5020 Salzburg, Austria  
E-mail: christian.prehal@plus.ac.at

S. Dörfler, H. Althues  
Department Battery Technology  
Fraunhofer Institute for Material and Beam Technology (IWS)  
Winterbergstraße 28, 01277 Dresden, Germany

H. Amenitsch  
Institute of Inorganic Chemistry  
Graz University of Technology  
Stremayrgasse 9, 8010 Graz, Austria

C. Zaubitzer  
Department of Chemistry and Applied Biosciences  
Scientific Center for Optical and Electron Microscopy  
ETH Zürich  
Otto-Stern-Weg 3, 8093 Zürich, Switzerland

 Supporting information for this article is available on the WWW under <https://doi.org/10.1002/batt.202500428>

 © 2025 The Author(s). *Batteries & Supercaps* published by Wiley-VCH GmbH. This is an open access article under the terms of the Creative Commons Attribution License, which permits use, distribution and reproduction in any medium, provided the original work is properly cited.

## 1. Introduction

Operando characterization techniques are essential for understanding the complex physicochemical processes governing electrochemical energy storage systems.<sup>[1]</sup> Enabling real-time observation of structural and chemical transformations, they provide important insights unavailable from traditional ex situ methods.<sup>[2–5]</sup> This capability is especially valuable for probing dynamic interfaces,<sup>[6]</sup> phase transformations,<sup>[7–10]</sup> and transport phenomena<sup>[7]</sup> in next-generation battery systems, from nano to micrometer length scales.

Among these methods, synchrotron-based X-ray techniques have revolutionized our understanding of conventional batteries, owing to their nondestructive nature, penetrating power, and multiscale analytical capabilities. For instance, XRD reveals phase transformation mechanisms in Li-ion electrodes,<sup>[11–13]</sup> while small-angle X-ray scattering (SAXS) provides important insights into morphological evolution and interfaces across battery technologies.<sup>[11,14]</sup> Applied to liquid electrolytes, these techniques identified rate-limiting steps and degradation mechanisms in Li-ion batteries,<sup>[15–20]</sup> elucidated reaction mechanisms in Li-S systems,<sup>[9,21–23]</sup> and revealed performance-limiting reaction product distributions and diffusion pathways in Li-air cells.<sup>[8,24]</sup> Such discoveries have directly spurred improvements in energy density, cycle life, and rate capability across multiple battery chemistries.

Despite the success in liquid-electrolyte systems, extending operando synchrotron X-ray techniques to all-solid-state battery

(ASSB) configurations presents substantial experimental hurdles.<sup>[25]</sup> Conventional cell designs are ill-suited for ASSB architectures, which often incorporate highly absorbing materials (e.g., indium anodes, certain solid electrolytes) and require sustained mechanical pressure to ensure interfacial contact and ionic conductivity.<sup>[26]</sup> Furthermore, the inherent spatial heterogeneity and dynamic evolution of interfaces within solid-state stacks would benefit from characterization methods capable of resolving structural and morphological transformations layer-by-layer during operation.<sup>[25]</sup> Designing suitable operando cells thus involves a difficult balance between maintaining mechanical integrity under the high pressures required for ASSBs,<sup>[26]</sup> ensuring proper electrochemical function, and achieving sufficient X-ray transparency. While progress has been made, for instance, with adaptations enabling reflection X-ray measurements (often based on coin cell geometry), these typically probe only near-surface regions,<sup>[27–30]</sup> missing bulk information. Extending X-ray analysis to the bulk via transmission, however, proves particularly demanding within the constrained environment of an operating ASSB. One common configuration is the through-plane geometry, where the X-ray beam travels perpendicular to the electrode layers (parallel to the pressure axis), often seen in adaptations of coin cell designs.<sup>[31]</sup> This approach is challenged by the total X-ray absorption through the entire stack thickness and potential limitations on pressure application imposed by X-ray transparent windows. An alternative is the cross-sectional geometry, where the beam travels parallel to the electrode layers (perpendicular to the pressure axis), allowing individual layers like the anode, separator, and cathode to be probed distinctly along the beam path. However, previous designs employing this cross-sectional approach often featured large stack diameters to accommodate sealing and pressure application.<sup>[32]</sup> Consequently, characterization typically relied on techniques utilizing highly penetrating radiation, such as high-energy X-ray diffraction or neutron-based methods (including imaging and tomography).<sup>[33–36]</sup> While advancements continue, achieving optimal performance and analysis remains difficult across different configurations. For instance, even recent through-plane transmission cells operate at lower pressures than ideal, impacting electrochemical behavior, reflected in factors such as reduced capacity and the need to employ very low cycling rates (e.g., C/60) for stable operation during measurement.<sup>[31]</sup>

Taken together, these challenges highlight a critical need in the field: an operando cell design that can simultaneously (1) provide cross-sectional X-ray beam access to individual battery layers, (2) maintain the high, uniform pressures required for realistic solid-state operation, and (3) be compatible with standard synchrotron small- and wide-angle X-ray scattering (SAXS/WAXS) capabilities without relying solely on highly penetrating radiation. To address these methodological limitations, we present a novel operando cell design specifically engineered for spatially-resolved X-ray scattering studies of solid-state batteries during electrochemical cycling. Key innovations include: (1) a cell geometry that enables cross-sectional X-ray measurements, providing direct access to individual battery layers and (2) a mechanical design that maintains the high pressures required for solid-state operation while ensuring X-ray transparency.

This configuration enables scanning operando SAXS/WAXS, a technique that combines spatial mapping with time-resolved SAXS/WAXS data, typically conducted on a Synchrotron X-ray scattering beamline. Each pixel in the resulting dataset contains atomic- and nanoscale structural information from SAXS/WAXS patterns collected throughout battery cycling. We demonstrate the capabilities of our setup using all-solid-state lithium-sulfur batteries (ASSLSB), a model system characterized by substantial volume changes and complex phase transformations. These features present significant challenges for operando characterization and underscore the value of our approach.<sup>[37–39]</sup> Our spatially-resolved SAXS/WAXS measurements during electrochemical operation reveal pronounced heterogeneities in Li<sub>2</sub>S phase evolution and morphology across the electrode stack, insights inaccessible via conventional bulk techniques. The measurements are complemented by operando scanning SAXS/WAXS measurements on a liquid-electrolyte Li-S system using a laboratory SAXS/WAXS system. This proves the principal functionality of the cell design for a variety of battery systems and experimental setups.<sup>[2–5]</sup>

## 2. Experimental Section

### 2.1. X-ray Scattering Measurement

#### 2.1.1. Synchrotron

Operando SAXS/WAXS experiments were conducted at the Austrian SAXS beamline at the Elettra Sincrotrone Trieste, utilizing a monochromatic X-ray beam with an energy of 16 keV to probe the structural evolution of solid-state Li-S batteries during operation. This high-energy beam combined with the high flux of the synchrotron was essential for achieving sufficient transmission through the highly attenuating solid-state cell assembly. The beam was focused to an 88 × 1000 μm<sup>2</sup> rectangular spot, allowing a reasonable spatial resolution across the electrode stack. Scattering data were collected using a Dectris Pilatus 1 M detector positioned at a sample-to-detector distance of 180 cm for SAXS, and a Dectris Pilatus 100K detector at a distance of 11.4 cm for WAXS, optimized for tracking both nanoscale and atomic-scale structural changes over a q-range of 0.03–6.71 nm<sup>-1</sup> and 16.9–34.7 nm<sup>-1</sup>, respectively. The experimental setup is illustrated in Figure 1a, where the X-ray beam passes through the operando cell, and the scattered signal is recorded on a 2D detector. The acquisition time per pixel is 7 s, and the cells are cycled at C/20.

#### 2.1.2. Lab-Scale

Scanning operando SAXS/WAXS measurements on the liquid cell setup were performed using a Xeuss 3.0 laboratory beamline (Xenocs). The instrument employed Cu K $\alpha$  radiation ( $\lambda = 1.54 \text{ \AA}$ ), collimated into a rectangular beam profile of 0.1 mm × 1.5 mm (height × width). The instrument's lower-energy Cu K $\alpha$  source is well-suited for measurements on the less-attenuating liquid-electrolyte cell assembly, but is insufficient for the highly

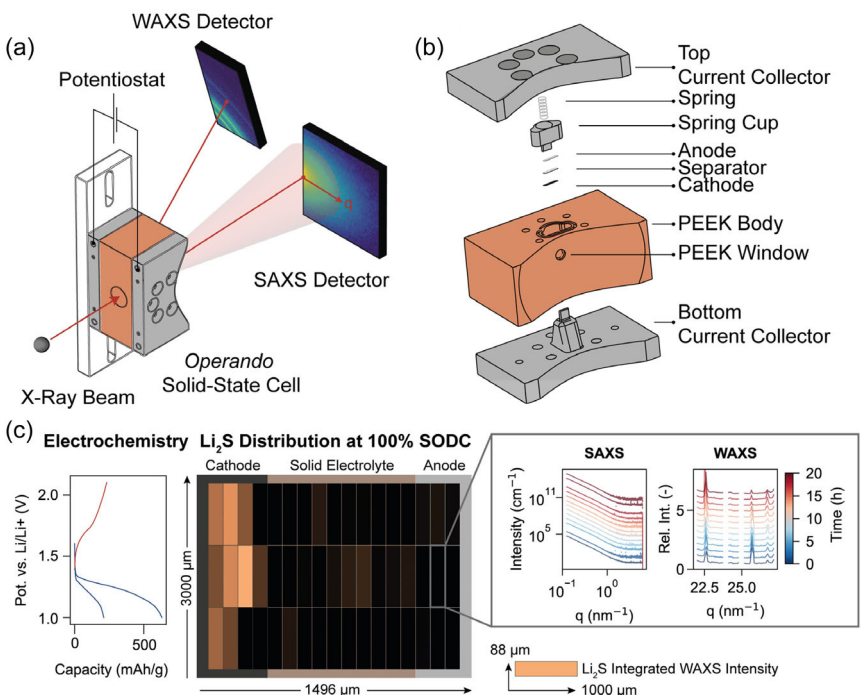


**Figure 1.** Spatially resolved operando SAXS/WAXS experiment and cell a) schematic illustration of the operando SAXS/WAXS experimental setup conducted at the ELETTRA synchrotron facility. b) Exploded view of the custom-designed operando cell, showing the stacked all-solid-state Li-S battery components. c) Electrochemical data with spatially-resolved  $\text{Li}_2\text{S}$  distribution after the first discharge, where each pixel represents fully time-resolved SAXS and WAXS spectra.

attenuating solid-state cell configuration. SAXS patterns were recorded using a DECTRIS Eiger2 1 M detector, positioned downstream from the sample. Simultaneously, WAXS patterns were recorded using a DECTRIS Eiger2 500k detector, placed closer to the sample in a transmission geometry setup. Spatially resolved data across the battery stack were acquired by scanning the cell through a  $5 \times 4$  measurement grid. The step size used was 1 mm (width) and 0.1 mm (height). The step size, along with the width, was selected to be less than the beam width of 1.5 mm, leading to an overlap between adjacent measurements in this dimension. This overlapping sampling approach provides spatial information potentially finer than the beam width along that axis. For each point (pixel) in the grid, SAXS and WAXS patterns were collected simultaneously with an exposure time of 80 s. This longer exposure time was necessary to compensate for the lower X-ray flux of the laboratory source and achieve an adequate signal-to-noise ratio.

## 2.2. Operando Battery Cell Design

The cell body was constructed in-house from polyetheretherketone (PEEK), chosen for its mechanical stability (tensile strength 97 MPa) and X-ray transparency. A PEEK window (thickness 500  $\mu\text{m}$ ) was precision-milled into the body over a rectangular active area aperture measuring 1  $\times$  5 mm to facilitate beam transmission. Effective sealing against the atmosphere was ensured using Viton O-rings, compressed as five M4 screws tightened

the stainless-steel current collectors against the PEEK body. The integrity of the sealing was confirmed by using lithium metal enclosed inside the cell. The cell was then exposed to ambient conditions for four days. Uniform stack pressure was maintained via a compression spring (DIN 2098/1 steel,  $k = 28.42 \text{ N mm}^{-1}$ , Kubo Tech AG) housed in a spring cup assembly. Electrical connection was made flexible through several cutouts (4 and 2 mm holes) in the current collectors, visible in Figure 1a. For measurement, the cell was mounted onto an insulating acrylic glass base (also visible in Figure 1a) via two M4 screws, isolating the bottom current collector from the conductive sample stage. The complete cell hardware architecture, illustrating the screwed assembly, is detailed in Figure 1b.

## 2.3. Battery Preparation

### 2.3.1. Solid-State Cell Assembly and Composition

All cell assembly steps were conducted in an argon-filled glovebox ( $\text{O}_2, \text{H}_2\text{O} < 0.1 \text{ ppm}$ ). The battery stack comprised a Li-In alloy anode, a  $\text{Li}_6\text{PS}_5\text{Cl}$  solid electrolyte separator (NEI Corporation, ionic conductivity  $3 \text{ mS cm}^{-1}$ ), and a templated carbon-sulfur composite cathode. The cathode composite was prepared with a mass ratio of 50:30:20 for  $\text{Li}_6\text{PS}_5\text{Cl}$  solid electrolyte, sulfur (99.998%, Sigma Aldrich), and CNovel-MH templated carbon (CABOT Corp.), respectively. To ensure precise cathode shape and placement within this constrained geometry, the freestanding cathode sheet was first positioned over the cell body aperture. The

bottom current collector was then carefully inserted into the PEEK body from below. This action simultaneously punched a cathode layer of the required 1 x 5 mm dimensions from the sheet and seated it firmly within the aperture, aligned with the X-ray windows. Excess cathode material outside the aperture was left in place to prevent disturbance of the positioned composite.

The Li-In anode was prepared using a standard procedure intended to form a thermodynamically stable two-phase mixture of indium and an InLi phase, which provides a stable potential plateau.<sup>[40]</sup> For the preparation, a specialized stainless-steel pellet press was developed (Figure S6, Supporting Information) to achieve the required pressures exceeding the tensile strength of PEEK. Initially, 6 mg of Li<sub>6</sub>PS<sub>5</sub>Cl solid electrolyte was pressed at 25 MPa to form a foundation pellet. Subsequently, layers of indium foil (100 µm) and lithium metal (50 µm) were added, and the complete stack was compressed at 400 MPa for 10 min to form the Li-In alloy anode pellet.

The cell assembly was completed by adding 2 mg of Li<sub>6</sub>PS<sub>5</sub>Cl solid electrolyte above the prepositioned cathode to establish ionic contact with the preformed anode pellet. This assembly was pressed at 90 MPa for 5 min. Finally, the spring cup was positioned, and the cell was sealed with the compression spring providing an operational pressure of 25 MPa during cycling.

The tensile strength of the PEEK cell body is approximately 110 MPa. To avoid strong plastic deformation of the thin X-ray window, the final in-cell assembly pressure was limited to 90 MPa. Consequently, higher-pressure steps, such as the initial 400 MPa anode formation, were necessarily performed in a separate, external pellet press (Figure S6, Supporting Information). Further, the precision tolerance of spring cup had to be increased to 100 µm to reduce friction forces between spring cup and PEEK body which in turn could lower the stack pressure. The spring-based mechanical assembly was chosen specifically to maintain a constant applied force on the battery stack throughout the experiment. This design compensates for the volume changes inherent to the active materials during electrochemical cycling. In contrast, a fixed-volume cell would lead to pressure fluctuations, which can be detrimental to the performance and lifetime of all-solid-state batteries.<sup>[41–43]</sup>

### 2.3.2. Liquid Cell Assembly and Composition

A freestanding cathode sheet was prepared using Ketjenblack carbon ECP-600JD (KB, Beyond Battery) and sulfur (S, 99.98% Sigma Aldrich) in a 2:1 weight ratio, mixed with 10 wt.% polytetrafluoroethylene (PTFE, Sigma Aldrich) mixed in water as a binder. The cathode was position punched into the cell the same way the solid system was done. Subsequently, three separator layers (two layers of Freudenberg glass fiber separator overlaid with one layer of polyethylene (PE) for mechanical stability) were placed onto the cathode. The separator stack was then wetted with 5 µL of electrolyte composed of 1 M bis(trifluoromethanesulfonyl)imide (LiTFSI, anhydrous, 99.99%) in 1:3 (v/v) 1,3-dioxolane (DOL, anhydrous, 99.5%, Sigma Aldrich) / 1,2-dimethoxy ethane (DME, anhydrous, 99.5%, Sigma Aldrich). For the anode, a

rectangular piece was cut from 50 µm thick lithium metal foil. This foil piece was carefully smoothed onto the flat face of the spring-loaded top current collector/plunger to ensure good contact and planarity. This entire top plunger assembly, carrying the Li foil anode, was then lowered onto the wetted separators to complete the cell stack. The assembled cell was cycled galvanostatically at a rate of C/20.

### 2.4. X-ray Data Processing

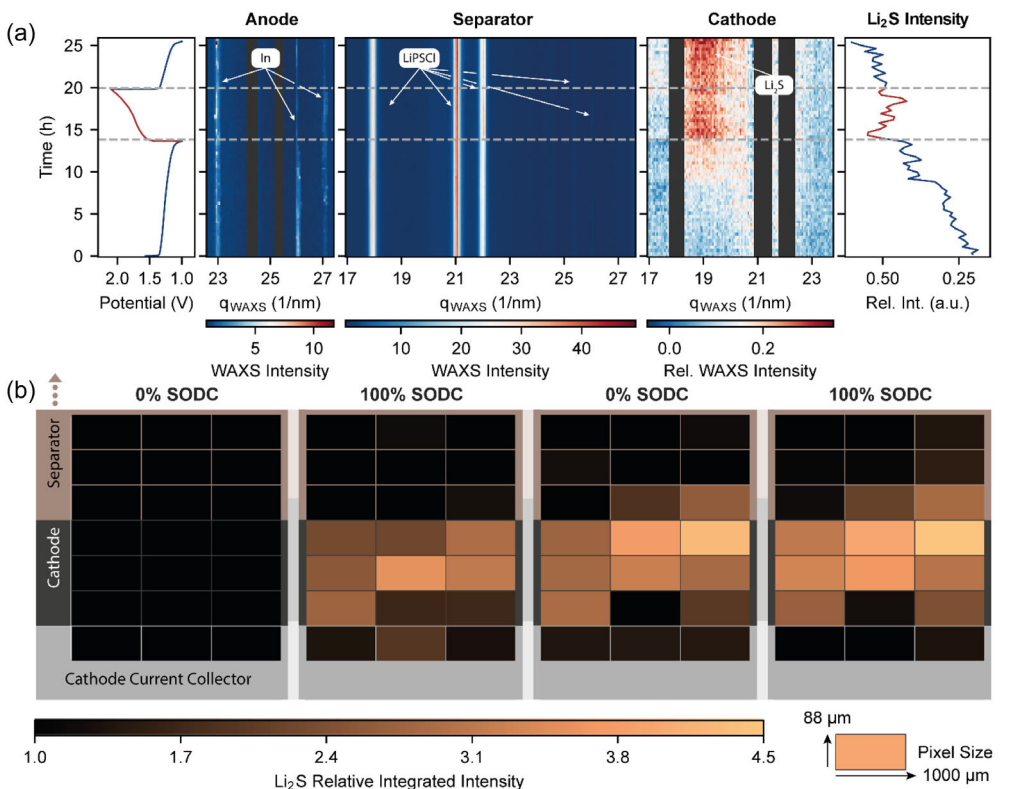
Initial alignment of the measurement grid relative to the battery components was done with vertical and horizontal X-ray transmission intensity scans to map the stack extent. A grid of measurement points ('pixels', corresponding to the 88 x 1000 µm<sup>2</sup> focused beam spot) was defined across the cell area for scanning SAXS/WAXS data acquisition. At each pixel, the full dataset comprising time-resolved SAXS and WAXS patterns was collected synchronously with the overall electrochemical cycling profile (voltage vs. capacity). The raw 2D scattering patterns collected at each time step and pixel were azimuthally integrated to obtain 1D intensity profiles ( $I(q)$ ). Background subtraction was performed using data from an empty cell measurement. To enhance the visibility of Li<sub>2</sub>S peak changes in the cathode WAXS data, patterns were normalized by dividing by the average intensity measured during the initial open-circuit voltage period. For the liquid cell experiment, the SAXS data was normalized to the intensity curve measured at the end of the first discharge plateau, corresponding to a state after sulfur dissolution but before significant Li<sub>2</sub>S formation.

Figure 1c illustrates the multidimensional nature of the collected data. The map in the center displays the relative spatial distribution of Li<sub>2</sub>S across the scanned area at the end of the first discharge (100% SODC), generated by integrating the intensity of the Li<sub>2</sub>S WAXS peak (centered near  $q = 19.8 \text{ nm}^{-1}$ ) over the range 18.3–20.8 nm<sup>-1</sup> for each pixel at that specific time point and normalizing relative to the initial state. The panel on the right exemplifies the rich, time-resolved information contained within each representative pixel: it shows the evolution of the SAXS and WAXS profiles presented here as waterfall plots (Intensity vs.  $q$ , with individual spectra offset and colored according to acquisition time) during electrochemical cycling (potential vs. capacity shown on the left).

## 3. Results and Discussion

### 3.1. Spatially Resolved Operando WAXS Analysis Reveals Dynamic Evolution of Battery Components

The operando scanning SAXS/WAXS technique enables simultaneous tracking of structural changes across all components of the solid-state Li-S battery during electrochemical cycling. Figure 2a presents the time-resolved WAXS patterns collected and averaged from distinct regions of the cell (anode, separator, and cathode) aligned with the electrochemical potential profile.



**Figure 2.** Spatially resolved operando WAXS measurement. a) Evolution of WAXS intensity over time during cell operation, showing phase changes in the anode, separator, and cathode. The leftmost panel displays the potential profile, while the rightmost panel presents the relative integrated intensity of Li<sub>2</sub>S formation. b) Spatial distribution of Li<sub>2</sub>S at different states of discharge (SODC), illustrating localized Li<sub>2</sub>S formation within the cathode region. The intensity scale represents the relative integrated Li<sub>2</sub>S signal (18.3–20.8 nm<sup>-1</sup>), highlighting variations in deposition.

This dataset reveals a number of chemical and structural transformations occurring throughout the cell architecture. A comprehensive analysis of an identical sister cell can be found in Figure S1, Supporting Information.

Detailed operando structural analysis of the Li–In alloy anode within a solid-state battery has been limited due to experimental difficulties probing it under realistic conditions.<sup>[40,44]</sup> Consequently, the reported mechanisms relied on liquid-electrolyte cells to study the alloy's phase evolution. However, these setups are faced with their own issues, such as unstable Li–In interface in liquid electrolytes.<sup>[44]</sup> Our operando cell design overcomes this barrier and enables direct observation of the anode in its native all-solid-state environment. Our WAXS data show that the anode is best described as a reactive, heterogeneous composite.<sup>[40]</sup> Throughout cycling, diffraction peaks from crystalline indium (In(101) reflection at  $q = 23.0 \text{ nm}^{-1}$  and In(002) at  $27.4 \text{ nm}^{-1}$ )<sup>[44]</sup> remain present. Yet, no distinct peaks for crystalline LiIn phases are observed, suggesting the LiIn product forms in an amorphous or highly nanocrystalline state.

The most direct evidence for the alloying reaction is the dynamic behavior of the In peaks themselves. The intensity of the In(101) and In(002) reflections varies during cycling. These intensity changes correlate with the charge/discharge state and suggest reversible lithiation/delithiation processes within the alloy. These intensity variations are aligned with the expected

reversible (de-)lithiation processes.<sup>[40]</sup> Interestingly, the In(110) reflection at  $q = 26.2 \text{ nm}^{-1}$  becomes narrow and weaker in intensity or disappears completely in the sister cell (Figure S1a, Supporting Information) immediately upon initial lithiation. This behavior suggests a preferential lithium insertion mechanism that anisotropically disrupts the crystallographic ordering associated with the (110) planes within the indium lattice, while maintaining partial ordering in other crystallographic directions. Understanding this actual structural state is important, as efficient Li<sup>+</sup> transport must overcome the relatively ion-blocking nature of pure indium by leveraging the properties of the formed LiIn phase, whether crystalline or amorphous.<sup>[45]</sup>

In contrast to the dynamic changes observed in the anode, the solid electrolyte separator region displays relatively stable diffraction patterns throughout cycling, with the primary Li<sub>0.5</sub>PS<sub>5</sub>Cl reflections maintaining consistent positions and intensities. The missing variability confirms the structural stability of the argyrodite phase during battery operation. Minor variations in peak intensities are observed (detailed in Figure S2, Supporting Information), which may indicate subtle reorganization of the electrolyte structure in response to local stress fields or electrochemical gradients.

The most pronounced structural changes occur within the cathode composite, where the formation and dissolution of

crystalline Li<sub>2</sub>S during discharge and charge cycles can be clearly tracked. The appearance of the Li<sub>2</sub>S diffraction peak at  $q = 19.8 \text{ nm}^{-1}$  correlates directly with the discharge process, reaching maximum intensity at full discharge. The integrated intensity of this peak, derived from normalized WAXS patterns (see Methods for details and rightmost panel in Figure 2a), provides a quantitative measure of Li<sub>2</sub>S formation kinetics throughout cycling. During charging, the Li<sub>2</sub>S integrated intensity signal diminishes as the discharge product is converted back to sulfur, though only  $\approx 37\%$  of the discharge capacity is recovered. This limited charging capacity is in line with other operando ASSB systems<sup>[31,35,36]</sup> and likely stems from a combination of factors specific to operando cells, including contact loss due to volume changes, insufficient stack pressure, and high interfacial resistance at solid–solid interfaces.<sup>[38]</sup> Mechanistically, this is consistent with sluggish ion transport within the thick composite cathode, a phenomenon that can lead to nonuniform delithiation and leave regions of active material ionically isolated from the separator during the charging process. The subsequent discharge capacity matches the charging capacity, confirming that the charging step is the limiting factor in the electrochemical reversibility.

Figure 2b further elucidates the spatial distribution of Li<sub>2</sub>S formation across the electrode stack at different states of discharge (SDOC), with intensities normalized to the initial state (0% SDOC) to account for any variations in the initial cell configuration. At 0% SDOC (fully charged state), no Li<sub>2</sub>S signal is detected throughout the cell. As discharge progresses to 100% SDOC, a heterogeneous distribution of Li<sub>2</sub>S emerges within the cathode region, with higher intensities observed in the central region of the cathode compared to regions near the current collector or separator interfaces, suggesting that parts of the cathode are not well ionically or electronically connected. During the subsequent charge cycle (0% SDOC), the Li<sub>2</sub>S signal decreases only slightly in most pixels, indicating limited delithiation of the formed Li<sub>2</sub>S. Concurrently, an increase in scattering intensity is observed in the pixels near the cathode–separator interface within the  $q$ -region associated with Li<sub>2</sub>S. The origin of this counter intuitive signal increase during Li<sub>2</sub>S consumption is uncertain. We hypothesize that this is caused by heterogeneous volume contraction during charging. Regions of the cathode with efficient delithiation (Li<sub>2</sub>S  $\rightarrow$  S) may shrink, while adjacent poorly-connected regions remain static. This differential strain could physically displace residual, unreacted Li<sub>2</sub>S particles from a contracting pixel volume into a neighboring one, leading to a net increase in measured Li<sub>2</sub>S intensity in that specific location. Such differential behavior could be amplified by inhomogeneous pressure gradients from the cell assembly, which would also contribute to variations in local ionic contact and electrochemical activity. However, scattering contributions from amorphous side-reaction products formed at the interface or artifacts from slightly imprecise background subtraction could explain the Li<sub>2</sub>S intensity increase at the interface. This increase at the interface is even more evident in the identical sister cell (Figure S1b, Supporting Information), which exhibits both a sharp decrease in Li<sub>2</sub>S intensity near the current collector and

a simultaneous increase in the separator region during charging. This may indicate partial detachment of the electrode from the current collector due to chemo-mechanical stress.

Complementary cryoFIB-SEM imaging (Figure S3, Supporting Information) provides insights into the microstructural origins of this heterogeneous reaction distribution. The cross-sectional analysis reveals significant variations in the spatial distribution of solid electrolyte and active material throughout the cathode composite. Regions with higher electrolyte concentration enable better Li<sup>+</sup> transport but contain less active material for conversion, while sulfur-rich domains may suffer from transport limitations despite their higher theoretical capacity. This inherent microstructural heterogeneity, combined with mechanical degradation during cycling, creates preferential reaction pathways that manifest in the spatially-resolved operando measurements.

### 3.2. SAXS Analysis Reveals Sulfur Conversion Mechanism in Tempered Carbon

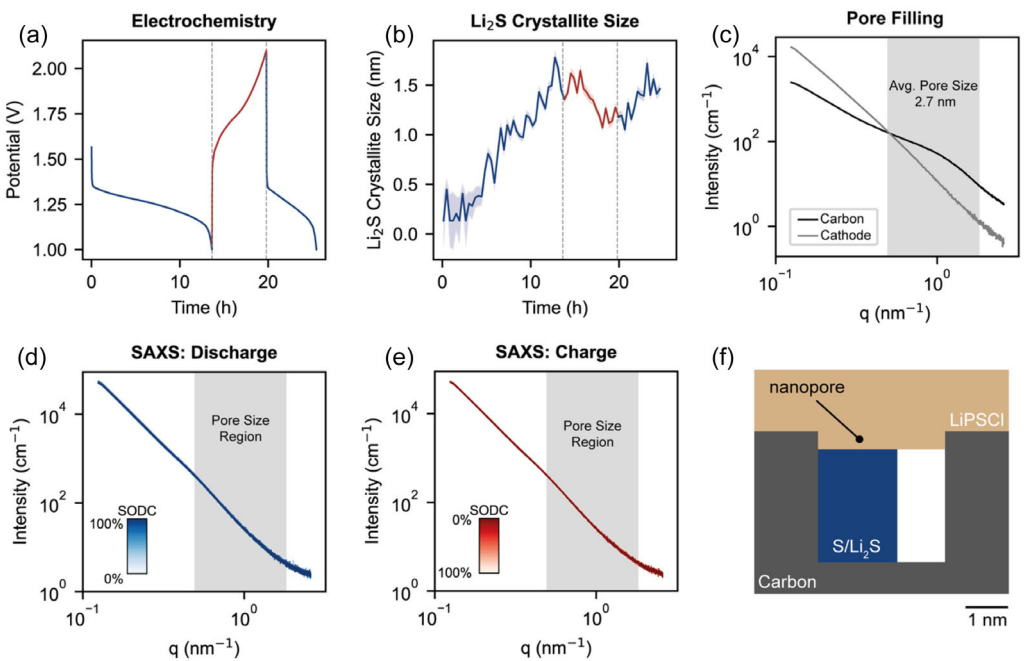
Beyond mapping the spatial distribution of crystalline phases, complementary SAXS data offer insight into the sulfur conversion mechanism within the carbon host. Fiedler et al. proposed that sulfur resides mainly on external surfaces or in larger pores, with smaller pores serving conductive roles.<sup>[38]</sup> Our time-resolved SAXS data allows us to explore whether the conversion occurs primarily on external carbon surfaces or within the carbon nanopore network.

Figure 3 presents time-resolved SAXS data collected during galvanostatic cycling, alongside the evolution of Li<sub>2</sub>S crystallite sizes derived from the diffraction peak width and the Scherrer equation. The WAXS data shows the formation of nanocrystalline Li<sub>2</sub>S during discharge. The Li<sub>2</sub>S crystallites reach up to 1.75 nm in size and evolve throughout the electrochemical process (Figure 3a,b).

In contrast, the SAXS profiles remain stable throughout cycling, particularly in the region corresponding to the templated carbon's nanoporous structure ( $\approx 2.7 \text{ nm}$  on average, Figure 3b). While interpreting stable scattering data requires caution, several arguments are in line with sulfur-to-sulfide conversion occurring within the nanopores.

#### 3.2.1. Initial Pore Filling

A comparison between the SAXS pattern of the pristine carbon host and that of the composite cathode (Figure 3c) shows the disappearance of the characteristic nanopore scattering feature upon sulfur infiltration. This indicates that sulfur preferentially fills the carbon nanopores during the initial preparation. Since the SAXS intensity of these pores depends on the square of the electron density contrast between the carbon matrix and the nanopores, the infiltration of sulfur (whose electron density is closer to that of carbon) reduces this contrast, leading to a corresponding decrease in SAXS intensity.



**Figure 3.** Evolution of sulfur species and  $\text{Li}_2\text{S}$  formation in solid-state Li-S battery during galvanostatic cycling. a) Potential profile showing discharge (blue) and charge (red) cycles with vertical dotted lines marking key transition points. b) Evolution of  $\text{Li}_2\text{S}$  crystallite size determined from WAXS peak analysis, showing nucleation and growth during discharge followed by dissolution during charge. c) SAXS measurement of the pristine carbon and composite cathode. The characteristic hump around corresponding to the nanopores in the pristine carbon vanishes in the composite cathode. d) SAXS intensity profiles during discharge as a function of scattering vector  $q$ . The intensity within the scattering region associated with the mesopores (highlighted in gray) is stable throughout cycling despite significant chemical transformations. e) SAXS intensity profiles during charge, demonstrating similar stability to the discharge process. f) Schematic of S and  $\text{Li}_2\text{S}$  respectively confined by the nanopores in the templated carbon. The electrolyte covered nanopores ensure ionic conductivity.

### 3.2.2. Implications of SAXS Stability during Cycling

The stability of the SAXS signal during cycling (Figure 3d,e) is consistent with sulfur conversion happening inside the pores. Lithiation in and out of the pores provides only a small contrast (electron density difference) change between carbon and the filled pores. We expect only minimal changes in the SAXS pattern, even when S converts to  $\text{Li}_2\text{S}$  within the pores. Therefore, the observed lack of change fits well with our expectation for an intra-pore reaction and aligns with findings in microporous carbons (pore size  $< 1 \text{ nm}$ ) and carbonate electrolytes.<sup>[7]</sup>

### 3.2.3. Confinement Effects on $\text{Li}_2\text{S}$ Size

The  $\text{Li}_2\text{S}$  crystallite size determined by WAXS ( $\leq 1.75 \text{ nm}$ ) is significantly smaller than typically observed in liquid cells where  $\text{Li}_2\text{S}$  often forms on external carbon surfaces. This sub-2 nm size fits well within the carbon's average nanopore dimension ( $\approx 2.7 \text{ nm}$ ), suggesting that crystal growth may be limited by spatial confinement within the pores (Figure 3f).

These qualitative arguments are supported by electron density contrast calculations of the sulfur-filled carbon host (see Table 2, Supporting Information for details). The calculations show that while the initial filling of pores with sulfur significantly reduces the scattering contrast, the subsequent partial conversion to  $\text{Li}_2\text{S}$  during discharge is expected to decrease the carbon

contribution of the SAXS intensity by a factor of 0.75. The significant and constant scattering contribution from other solid-state components leads to a relative SAXS intensity change that is even smaller. Given the experimental signal-to-noise ratio, we believe that this small change is not visible on the logarithmic intensity scale and below the detection limit of our experiment, which is consistent with the observed stable SAXS signal.

To confirm that our operando setup possesses sufficient sensitivity to track nanoscale conversion processes and that the observed SAXS stability is a genuine feature of the solid-state system, we performed a control experiment using a liquid-electrolyte Li-S system where pronounced nanoscale changes are well-documented.<sup>[9,10]</sup> As detailed in the following section (and Figure 4), this experiment demonstrated that our cell design can indeed capture pronounced SAXS variations when present, thereby validating that the stability seen in the solid-state measurement reflects the actual confined reaction pathway rather than an experimental limitation.

### 3.3. Validating Cell Design with a Liquid Electrolyte Li-S System

To validate that our cell design can indeed capture SAXS signal changes when they occur, we adapted it for measurements on a conventional liquid-electrolyte Li-S battery (detailed in the

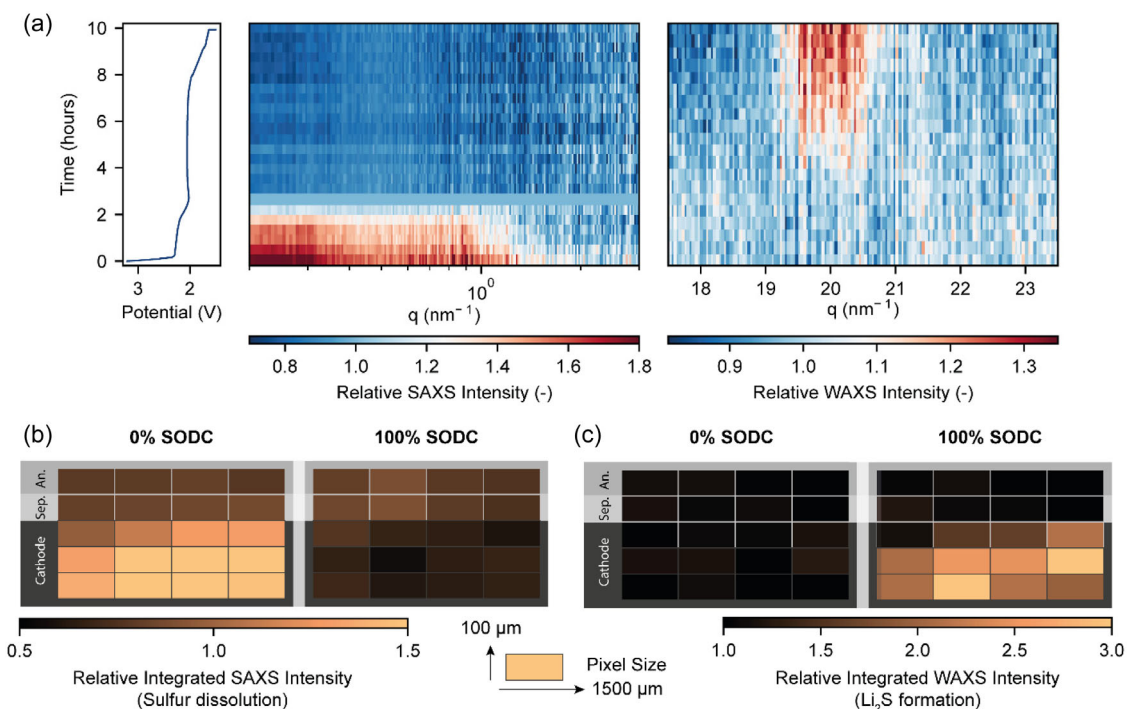


**Figure 4.** Operando S/WAXS imaging of a liquid electrolyte Li-S battery. a) Time-resolved SAXS (center) and WAXS (right) data during galvanostatic discharge with the corresponding voltage profile (left). The WAXS data shows the formation of  $\text{Li}_2\text{S}$  (peak at  $q = 19.8 \text{ nm}^{-1}$ ), while the SAXS data exhibits pronounced intensity changes in the low- $q$  region, indicating sulfur dissolution into the liquid electrolyte. b) Spatial distribution of S at 0% and 100% state of discharge (SODC) determined via integrated SAXS intensity ( $0.2\text{--}1 \text{ nm}^{-1}$ ), illustrating sulfur dissolution during discharge. c) Spatial distribution of  $\text{Li}_2\text{S}$  at 0% and 100% state of discharge (SODC) determined via integrated WAXS intensity ( $18.3\text{--}20.8 \text{ nm}^{-1}$ ), illustrating the evolution of discharge product formation across the cathode.

Supporting Information). This control experiment, presented in Figure 4, aimed to confirm whether the stable SAXS signal observed in the solid-state system (Figure 2, 3) represents a true mechanistic feature or an experimental limitation. In contrast to the solid-state experiments, these validation measurements were successfully performed using a laboratory-based Xenocs Xeuss 3.0 SAXS instrument, demonstrating the versatility of the cell design.

Figure 4a displays the time-resolved WAXS and SAXS data collected during partial discharge of the liquid-electrolyte cell. As expected for liquid Li-S systems, the normalized SAXS profiles (see Methods for details) exhibit pronounced intensity variations in the beginning of the discharge, particularly visible in the  $q$ -range of  $0.1\text{--}1 \text{ nm}^{-1}$ . This significant change in scattering intensity directly corresponds to the well-established dissolution of sulfur in the liquid electrolyte,<sup>[9,10]</sup> a process completely absent in the solid-state configuration. The dissolution creates substantial changes in the nanoscale contrast profile as solid sulfur transitions to soluble polysulfide species, confirming our cell's capability to detect such phenomena when present.

At the same time, the WAXS data shows the formation of  $\text{Li}_2\text{S}$  during discharge with the appearance of characteristic diffraction peaks at  $q = 19.8 \text{ nm}^{-1}$ , further validating the cell's ability to capture crystalline phase evolution during electrochemical processes. The spatial mapping of sulfur and  $\text{Li}_2\text{S}$  distribution at different states of discharge (Figure 4c) demonstrates our

technique's capability to track reaction product dissolution and formation spatially across the electrode structure, even on lab-scale instruments.

The results from this liquid-electrolyte control experiment provide further support for our interpretation of the solid-state battery data. By capturing the expected, pronounced SAXS variations associated with sulfur dissolution, we confirm that our operando setup possesses the necessary sensitivity to detect such nanoscale changes. Therefore, the contrasting stability observed in the solid-state SAXS profiles (Figure 3c,d) can indeed be attributed to a fundamental mechanistic effect, rather than an experimental artifact.

Although we could not complete full cycling due to challenges with maintaining pressure, preventing dendrite formation, and balancing the liquid electrolyte volume (detailed in the Supporting Information and Figure S7), the partial discharge data were sufficient to achieve our main validation goal. This confirmation strengthens our analysis of the solid-state Li-S system's behavior.

## 4. Conclusion

Understanding the complex spatio-temporal dynamics within ASSBs during operation is critical, but difficult due to challenges in conducting operando scattering experiments under relevant

conditions. To address this, we developed a novel operando cell enabling spatially-resolved scanning SAXS/WAXS measurements perpendicular to the electrode stack while maintaining high pressure. This setup allows simultaneous, time-resolved mapping of the crystalline phases evolution (WAXS) and nanoscale structure changes (SAXS) across distinct battery layers.

Applying this technique to an all-solid-state Li-S model system revealed detailed insights. For instance, WAXS data from the anode side captured the structural evolution of the Li-In alloy, revealing anisotropic lithiation pathway through the preferential disruption of In(110) planes and suggesting the formation of an amorphous LiIn phase. WAXS data also revealed the spatially heterogeneous formation of  $\text{Li}_2\text{S}$  in the cathode during discharge, highlighting the impact of electrode architecture on reaction pathways. Stable SAXS profiles indicate the preservation of the nanopore/active materials structure during electrochemical cycling. The width of the  $\text{Li}_2\text{S}$  diffraction peaks indicates crystallite sizes smaller than 2 nm, consistent with the mean pore dimension of 2.7 nm. This suggests that sulfur conversion occurs primarily within the confinement of the templated carbon nanopores. These results demonstrate how spatially-resolved scattering uncovers reaction dynamics and confinement effects that remain hidden for many other techniques.

Control experiments on a liquid Li-S system corroborated the validity of these interpretations, particularly the genuineness of the stable SAXS signal in the solid-state system. In the liquid electrolyte system, SAXS revealed pronounced nanoscale structural changes during the initial discharge, consistent with sulfur dissolution and confirming the sensitivity of the SAXS signal to dynamic processes.

While this work demonstrates the potential of our approach, there are several points to be improved in future studies. The spatial resolution of the scanning set-up is limited by the available beam size. Using nano or microfocused X-ray beams at advanced beamlines can enable (sub-)micrometer resolutions in the future. Ensuring highly uniform pressure application across the stack and mitigating potential friction effects within the cell remains a challenge inherent to this design. Future iterations of the cell design could incorporate improvements such as diamond windows, which offer a lower X-ray background and higher mechanical strength, alongside modifications specifically targeting enhanced pressure homogeneity. Though this study focused on Li-S chemistry and included primarily qualitative SAXS/WAXS data analyses, the method is broadly applicable. Furthermore, the cell's transmission geometry makes it potentially suitable for other techniques, such as spatially-resolved X-ray absorption spectroscopy, although data quality may be impacted by background scattering from the PEEK window. Future work could integrate other ASSB chemistries, study long-term degradation, and combine the scattering analysis with quantitative modeling approaches.

In summary, the developed operando setup enables spatially and temporally resolved investigations of electrochemical phase transformation mechanisms in ASSBs, supporting the development of better materials and cell designs through a more detailed understanding.

## Acknowledgements

The authors acknowledge the funding for the ALISA project (project no. 9359) provided by the <http://m-ERA.NET> network (part of the European Union's Horizon 2020 research and innovation program (under grant agreement no. 958174)). J.M.M. and A.S.G. acknowledge the financial support for the ALISA project from the Swiss Federal Office of Energy SFOE. J.M.M highlights the invaluable help from Silvio Scherr with the cell's design and drawings and Valentino Anagua Suter with the manufacturing of all the parts. Additionally, J.M.M. mentions the valuable help from Mario Mücklich (ETH Zürich). Electron microscopy measurements were done at the Scientific Scenter for Optical and Electron Microscopy (ScopeM). This work is supported by the ERC starting grant SOLIDCON,101078271, funded by the European Union. Views and opinions expressed are, however, those of the authors only and do not necessarily reflect those of the European Union or the European Research Council Executive Agency. Neither the European Union nor the granting authority can be held responsible for them. The authors acknowledge the CERIC-ERIC Consortium for the access to the TUG Austrian SAXS beamline at ELETTRA and financial support.

## Conflict of Interest

The authors declares no conflicts of interest

## Data Availability Statement

The data that support the findings of this study are available at <https://doi.org/10.5281/zenodo.16755892>.

**Keywords:** all-solid-state battery · lithium · operando scattering · sulfur

- [1] X. Wei, X. Wang, Q. An, C. Han, L. Mai, *Small Methods* **2017**, *1*, 1700083.
- [2] S.-M. Bak, Z. Shadike, R. Lin, X. Yu, X.-Q. Yang, *NPG Asia Mater.* **2018**, *10*, 563.
- [3] D. Cheng, J. Hong, D. Lee, S.-Y. Lee, H. Zheng, *Chem. Rev.* **2025**, *125*, 1840.
- [4] Z. Lin, L. Qian, J. Yang, H. Lin, X. Wang, L. Wu, B. Yuan, L. Kang, J. Zhu, Y. Ren, Y. Ke, S. Han, *ACS Appl. Mater. Interfaces* **2025**, *17*, 11495.
- [5] L. Meyer, N. Sagib, J. Porter, *J. Electrochem. Soc.* **2021**, *168*, 090561.
- [6] J. Maibach, J. Rizell, A. Matic, N. Mozhzhukhina, *ACS Mater. Lett.* **2023**, *5*, 2431.
- [7] A. S. Gungor, J.-M. von Mentlen, J. G. A. Ruthes, F. J. García-Soriano, S. D.č Talian, V. Presser, L. Porcar, A. Vizintin, V. Wood, C. Prehal, *ACS Appl. Mater. Interfaces* **2024**, *16*, 67651.
- [8] C. Prehal, A. Samojlov, M. Nachtnebel, L. Lovicar, M. Kriechbaum, H. Amenitsch, S. A. Freunberger, *Proc. Nat. Acad. Sci.* **2021**, *118*, e2021893118.
- [9] C. Prehal, J.-M. von Mentlen, S. D.č Talian, A. Vizintin, R. Dominko, H. Amenitsch, L. Porcar, S. A. Freunberger, V. Wood, *Nat. Commun.* **2022**, *13*, 6326.
- [10] J.-M. von Mentlen, A. S. Gungor, T. Demuth, J. Belz, M. Plodinec, P. Dutta, A. Vizintin, L. Porcar, K. Volz, V. Wood, C. Prehal, *ACS Nano* **2025**, *19*, 16626.
- [11] W. Cheng, M. Zhao, Y. Lai, X. Wang, H. Liu, P. Xiao, G. Mo, B. Liu, Y. Liu, *Exploration* **2024**, *4*, 20230056.
- [12] M. Pin, J. Choi, J. H. Chang, A. S. Schenk, J. Han, S. Waclawek, Y. Kim, J. Y. Cheong, *Energy Storage Mater.* **2024**, *73*, 103798.

- [13] L. Fang, R. E. Winans, T. Li, *Nano Energy* **2024**, *121*, 109255.
- [14] J. Lee, H. Park, H. Kim, T. Kim, M. Jin, T. Kim, J. M. Kim, *Bull. Korean Chem. Soc.* **2023**, *44*, 452.
- [15] J. Hu, B. Wu, X. Cao, Y. Bi, S. Chae, C. Niu, B. Xiao, J. Tao, J. Zhang, J. Xiao, *J. Power Sources* **2020**, *454*, 227966.
- [16] M. Hess, T. Sasaki, C. Villevieille, P. Novák, *Nat. Commun.* **2015**, *6*, 8169.
- [17] A. Senyshyn, O. Dolotko, M. J. Mühlbauer, K. Nikolowski, H. Fuess, H. Ehrenberg, *J. Electrochem. Soc.* **2013**, *160*, A3198.
- [18] S. Takagi, K. Shimoda, H. Kiuchi, K. Hase, Z. Ogumi, T. Abe, *Carbon N.Y.* **2025**, *238*, 120204.
- [19] H. He, C. Huang, C.-W. Luo, J.-J. Liu, Z.-S. Chao, *Electrochim. Acta* **2013**, *92*, 148.
- [20] J. S. Edge, S. O'Kane, R. Prosser, N. D. Kirkaldy, A. N. Patel, A. Hales, A. Ghosh, W. Ai, J. Chen, J. Yang, S. Li, M.-C. Pang, L. B. Diaz, A. Tomaszewska, M. W. Marzook, K. N. Radhakrishnan, H. Wang, Y. Patel, B. Wu, G. J. Offer, *Phys. Chem. Chem. Phys.* **2021**, *23*, 8200.
- [21] S. Huang, L. Liu, Y. Wang, Y. Shang, L. Zhang, J. Wang, Y. Zheng, O. G. Schmidt, H. Y. Yang, *J. Mater. Chem. A Mater.* **2019**, *7*, 6651.
- [22] G. Tonin, G. B. M. Vaughan, R. Bouchet, F. Alloin, M. Di Michiel, C. Barchasz, *J. Power. Sources* **2020**, *468*, 228287.
- [23] S.-H. Yu, X. Huang, K. Schwarz, R. Huang, T. A. Arias, J. D. Brock, H. D. Abrúñia, *Energy Environ. Sci.* **2018**, *11*, 202.
- [24] C. Prehal, S. Mondal, L. Lovicar, S. A. Freunberger, *ACS Energy Lett.* **2022**, *7*, 3112.
- [25] E. P. Alsaç, D. L. Nelson, S. G. Yoon, K. A. Cavallaro, C. Wang, S. E. Sandoval, U. D. Eze, W. J. Jeong, M. T. McDowell, *Chem. Rev.* **2025**, *125*, 2009.
- [26] A. Joshi, D. K. Mishra, R. Singh, J. Zhang, Y. Ding, *Appl. Energy* **2025**, *386*, 125546.
- [27] B. Aktekin, E. Kataev, L. M. Riegger, R. Garcia-Diez, Z. Chalkley, J. Becker, R. G. Wilks, A. Henss, M. Bär, J. Janek, *ACS Energy Lett.* **2024**, *9*, 3492.
- [28] A. M. Stavola, E. K. Zimmerer, X. Sun, K. C. Wawer, A. M. Kiss, T. Ji, H. Zhu, J. W. Gallaway, *J. Electrochem. Soc.* **2024**, *171*, 030501.
- [29] X. Liu, D. Wang, G. Liu, V. Srinivasan, Z. Liu, Z. Hussain, W. Yang, *Nat. Commun.* **2013**, *4*, 2568.
- [30] A. L. Davis, E. Kazyak, D. W. Liao, K. N. Wood, N. P. Dasgupta, *J. Electrochem. Soc.* **2021**, *168*, 070557.
- [31] K. Choudhary, I. O. S. Mendoza, A. Nadeina, D. Becker, T. Lombard, V. Seznec, J.-N. Chotard, *J. Power Sources* **2023**, *553*, 232270.
- [32] D. Cao, Y. Zhang, T. Ji, H. Zhu, *MRS Bull.* **2023**, *48*, 1257.
- [33] X. Sun, A. M. Stavola, D. Cao, A. M. Bruck, Y. Wang, Y. Zhang, P. Luan, J. W. Gallaway, H. Zhu, *Adv. Energy Mater.* **2021**, *11*, 2002861.
- [34] S. Lou, Z. Yu, Q. Liu, H. Wang, M. Chen, J. Wang, *Chem* **2020**, *6*, 2199.
- [35] R. Bradbury, N. Kardjilov, G. F. Dewald, A. Tengattini, L. Helfen, W. G. Zeier, I. Manke, *Adv. Funct. Mater.* **2023**, *33*, 2302619.
- [36] R. Bradbury, G. F. Dewald, M. A. Kraft, T. Arlt, N. Kardjilov, J. Janek, I. Manke, W. G. Zeier, S. Ohno, *Adv. Energy Mater.* **2023**, *13*, 2203426.
- [37] S. Ohno, W. G. Zeier, *Acc. Mater. Res.* **2021**, *2*, 869.
- [38] M. Fiedler, M. A. Lange, F. Hippauf, S. Dörfler, H. Althues, W. G. Zeier, S. Kaskel, *Carbon N.Y.* **2024**, *227*, 119252.
- [39] M. Fiedler, S. Cangaz, F. Hippauf, S. Dörfler, T. Abendroth, H. Althues, S. Kaskel, *Adv. Sustainable Syst.* **2023**, *7*, 2200439.
- [40] A. L. Santhosha, L. Medenbach, J. R. Buchheim, P. Adelhelm, *Batter. Supercaps* **2019**, *2*, 524.
- [41] H. Q. Nguyen, M. D. Kanedal, J. Todt, F. Jin, Q. Do, D. Zalka, A. Maximenko, D. Stoian, N. Schell, W. van Beek, H. Fitzek, J. Rattenberger, V. Siller, S. T. Boles, M. E. Kazzi, J. Keckes, D. Rettenwander, *J. Am. Chem. Soc.* **2025**, *147*, 23492.
- [42] S. Mičík, E. Šimon, J. Todt, K. Végsö, P. Nádaždy, P. Krížik, E. Majková, J. Keckes, J. Li, P. Siffalovic, *Small* **2024**, *20*, 2307837.
- [43] C. Lee, J. Y. Kim, K. Y. Bae, T. Kim, S.-J. Jung, S. Son, H.-W. Lee, *Energy Storage Mater.* **2024**, *66*, 103196.
- [44] E. A. Il'ina, K. V. Druzhinin, E. D. Lyalin, M. S. Plekhanov, I. I. Talankin, B. D. Antonov, A. A. Pankratov, *J. Mater. Sci.* **2022**, *57*, 1291.
- [45] J. Aspinall, Y. Chart, H. Guo, P. Shrestha, M. Burton, M. Pasta, *ACS Energy Lett.* **2024**, *9*, 578.

---

 Manuscript received: June 2, 2025

Revised manuscript received: July 29, 2025

Version of record online: